

Inferring Granger Causality from Irregularly Sampled Time Series

Song Wei^a Yao Xie^a Christopher S. Josef^b Rishikesan Kamaleswaran^{c,d}

^aSchool of Industrial and Systems Engineering, Georgia Institute of Technology.

^bDepartment of Surgery, Emory University School of Medicine.

^cDepartment of Biomedical Informatics, Emory University School of Medicine.

^dDepartment of Biomedical Engineering, Georgia Institute of Technology.

June 7, 2021

Abstract

Continuous, automated surveillance systems that incorporate machine learning models are becoming increasingly more common in healthcare environments. These models can capture temporally dependent changes across multiple patient variables and can enhance a clinician’s situational awareness by providing an early warning alarm of an impending adverse event such as sepsis. However, most commonly used methods, e.g., XGBoost, fail to provide an interpretable mechanism for understanding why a model produced a sepsis alarm at a given time. The “black box” nature of many models is a severe limitation as it prevents clinicians from independently corroborating those physiologic features that have contributed to the sepsis alarm. To overcome this limitation, we propose a generalized linear model (GLM) approach to fit a Granger causal graph based on the physiology of several major sepsis-associated derangements (SADs). We adopt a recently developed stochastic monotone variational inequality-based estimator coupled with forwarding feature selection to learn the graph structure from both continuous and discrete-valued as well as regularly and irregularly sampled time series. Most importantly, we develop a non-asymptotic upper bound on the estimation error for any monotone link function in the GLM. We conduct real-data experiments and demonstrate that our proposed method can achieve comparable performance to popular and powerful prediction methods such as XGBoost while simultaneously maintaining a high level of interpretability.

1 Introduction

Automated surveillance tools aimed at identifying a patient’s deterioration inside the hospital are becoming more common and stand to enhance a clinician’s situational awareness; however, model predictions related to disease identification, particularly for complex diseases, still need to be adjudicated (i.e., interpreted) by a clinician before further action (i.e., treatment) can be initiated.

Sepsis is a life-threatening medical condition contributing to one in five deaths globally [WHO, 2020] and exists as one of the most important cases for automated in-hospital surveillance. Sepsis is formally defined as life-threatening organ dysfunction caused by a dysregulated host response to infection [Singer et al., 2016]. Delays in recognizing sepsis and initiating appropriate treatment can adversely impact patient outcomes. In a recent study of adult sepsis patients, each hour of delayed treatment was associated with higher risk-adjusted in-hospital mortality (odds ratio, 1.04 per hour) [Seymour et al., 2017]. It stands to reason that early recognition of the physiologic aberrations preceding sepsis would afford clinicians more time to intervene and may contribute to improving outcomes and reducing costs. A number of machine learning methods have been developed to predict the onset of sepsis utilizing data from the electronic medical record (EMR) [Fleuren et al., 2020]. A recent sepsis prediction competition [Reyna et al., 2019] demonstrated both the popularity and robust performance of XGBoost models [Du et al., 2019, Zabihi et al., 2019, Yang et al., 2020]; meanwhile, Deep Neural Networks [Shashikumar et al., 2021] are also commonly used. Regrettably, most approaches offer an alert adjudicator very little information pertaining to the reason for the alert/prediction, leading many to refer to them as “black box” techniques. Among the aforementioned works, Yang et al. [2020] provided one of the best attempts at identifying causality for their models’ predictions by reporting feature importance at a global level for all patients; however, this does not convey which features were most important in arriving at a given prediction for an individual patient. The common lack of interpretability of many clinical models, particularly those related to sepsis, suggests that a principled method (with theoretical guarantee) to study the interactions among time series in medical settings is underdeveloped.

Granger causal graphs, which analyze interactions among time series defined by association, avoid this limitation and afford a clinical adjudicator the ability to understand why an alert was made. The syndromic nature of sepsis means that there is a constellation of different physiologic derangements that can combine to create the condition. As evidenced in Figure 1, a series of different nodes representing these types of physiologic derangements has been created. The relationships between nodes and their effect on sepsis are explained via generalized linear models (GLM), providing insight into what “caused” the alert. For example, a clinical adjudicator might be more inclined to arrive at a concordant opinion regarding sepsis if they were informed that the alert

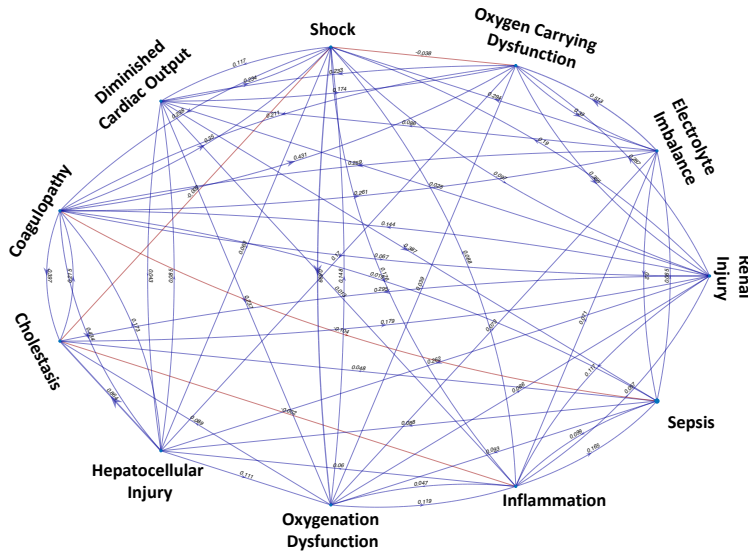


Figure 1: Granger Causal graph over endogenous Sepsis Associated Derangement (SAD) indicators obtained via discrete Hawkes network with forward feature selection.

was caused by the combined effects from the Renal Injury and Diminished Cardiac Output nodes. Likewise, this same adjudicator might be less inclined to corroborate an alert on a different patient if the main contributing cause was from Electrolyte Imbalance alone.

Linear Vector Autoregressive (VAR) model is the most popular method in studying the Granger causal graph among multiple time series [Lütkepohl, 2005]. However, it has been pointed out by a recent survey study [Shojaie and Fox, 2021] that this approach suffers from assumptions such as linearity and continuous-valued series, since the real-data, which can be both continuous- and categorical-valued, usually exhibits complex dynamics; another flaw of classic linear VAR model is unscalability to high-dimension, which arises when one tries to identify all series as endogenous, since it is hard to check if we have all relevant information at hand in practice.

In this work, we adopt a generalized linear model (GLM) approach for binary time series — spatio-temporal Bernoulli process [Juditsky and Nemirovski, 2019, Juditsky et al., 2020] — and generalize it to handle both continuous- and discrete-valued as well as regularly and irregularly sampled time series and learn a Granger causal graph over Sepsis Associated Derangements (SADs). We perform forward feature selection to remove redundant information and increase the signal-noise ratio. We demonstrate via real data experiments that our proposed GLM coupled with forward feature selection can achieve comparable performance to a powerful method such as XGBoost.

One novel aspect of this work comes from the real underlying problem: we build a *highly interpretable* model from *mixed-type series*. The prioritization of interpretability considers the needs of the end-users, namely clinicians. This consideration of real-world constraints makes

future adoption of these models much more likely for those conducting continuous surveillance of high-risk patients. In the medical setting, the observations can be both discrete and continuous-valued and sampled with different frequencies. For example, vital signs are recorded regularly, whereas laboratory (lab) tests are only ordered when clinically necessary; thus, this cannot be simply formulated into a missing data problem. Moreover, what separates our method from the classic linear VAR time series is the generalization to non-linear dynamics and a novel stochastic monotone variational inequality-based estimator. Most importantly, we develop a non-asymptotic upper bound on estimation error AND a Linear Program-based confidence interval for graph structure for arbitrary monotone (non-linear) link function for our proposed method.

Related work. Recent developments on the Granger causal graph mainly focus on non-linear dynamics and tackling high-dimensionality via regularization: the former includes applying a separable matrix-valued kernel [Sindhwani et al., 2012] and neural networks [Tank et al., 2018] to learn non-linear Granger causality; other approaches address the issue of high-dimensionality caused by viewing all series as endogenous. Techniques include group Lasso [Bolstad et al., 2011, Basu et al., 2015] and nuclear norm regularization [Basu et al., 2019]. Another notable work [Nicholson et al., 2017] modeled endogenous and exogenous variables separately (instead of treating all series endogenous) and used different penalties on endogenous and exogenous variables to learn the sparse graph structure. We should mention that our method closely resembles Nicholson et al. [2017]: part of features comes from direct observations and is treated exogenous (e.g., vital signs and Lab test results), whereas the remaining SADs are derived from the first part and viewed as endogenous.

2 Problem set-up and proposed model

2.1 Mixed-type series

Data used for this analysis was a curated, publicly available data set from the 2019 Physionet challenge [Reyna et al., 2020]. The challenge data was sourced from patients admitted to the Intensive Care Unit (ICU) during their hospitalization and represented three categories of patient features: vital sign measurements, Laboratory (Lab) results, and demographic information.

Vital Signs. Vital signs in ICU environments are normally recorded at an hourly interval and include HR, O2Sat, Temp, SBP, MAP, DBP, Resp (see Table 1 for their full measurement names). Among the blood pressure measurements (SBP, DBP, and MAP), we only keep MAP in our study since $MAP = (SBP + 2DBP)/3$.

Lab Values. Lab tests are most commonly collected once every 24 hours; however, this collection frequency may change based on the severity of a patient’s illness. In addition to individual Lab values,

we also use the count of the Lab tests over the past 6 hours as a proxy to represent the severity of a patient’s illness (i.e., more severe disease results in more tests being ordered).

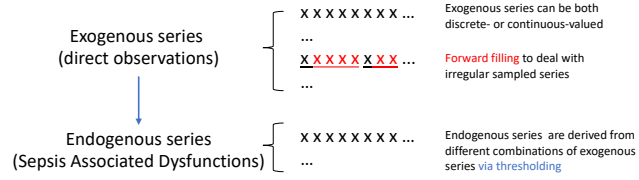
Sepsis Associated Derangements (SADs). Thresholds representing breaks between normal and deranged physiology are identified utilizing already establish criteria [ABIM]. We condense different measurements (containing both vital signs and Lab results) into a binary variable as an indicator of physiologic derangements seen preceding and during sepsis (see column “SAD name” in Table 1).

Table 1: SAD construction based on thresholding exogenous observations via medical knowledge.

SAD NAME	MEASUREMENT NAME	PHYSIONET NAME	RULE	RISK SCORE
RENAL INJURY	CREATININE	CREATININE	>1.3	0.667
	POTASSIUM	POTASSIUM	>5.0	0.067
	PHOSPHORUS	PHOSPHATE	>4.5	0.067
	BICARB (HCO3)	HCO3	>26	0.067
	BLOOD UREA NITROGEN (BUN)	BUN	>20	0.133
ELECTROLYTE IMBALANCE	CALCIUM	CALCIUM	>10.5	0.167
	CHLORIDE	CHLORIDE	<98 OR >106	0.667
	MAGNESIUM	MAGNESIUM	<1.6	0.167
OXYGEN CARRYING DYSFUNCTION	HEMATOCRIT	HCT	<37	0.500
	HEMOGLOBIN	HGB	<12	0.500
SHOCK	BASE EXCESS	BASEEXCESS	< -3	0.100
	LACTIC ACID	LACTATE	>2.0	0.150
	PH	PH	<7.32	0.750
DIMINISHED CARDIAC OUTPUT	SBP CUFF	SBP	<120	0.250
	DBP CUFF	DBP	<80	0.250
	MAP CUFF	MAP	<65	0.500
COAGULOPATHY	PARTIAL PROTHROMBIN TIME (PTT)	PTT	>35	0.250
	FIBRINOGEN	FIBRINOGEN	<233	0.250
	PLATELETS	PLATELETS	<150,000	0.500
CHOLESTASIS	BILIRUBIN DIRECT	BILIRUBIN DIRECT	>0.3	0.100
	BILIRUBIN TOTAL	BILIRUBIN TOTAL	>1.0	0.500
	ALKALINE PHOSPHATASE	ALKALINEPHOS	>120	0.400
HEPATOCELLULAR INJURY	ASPARTATE AMINOTRANSFERASE (AST)	AST	>40	1.000
OXYGENATION DYSFUNCTION	UNASSISTED RESP RATE	RESP	>20	0.100
	SPO2	O2SAT	<92 %	0.200
	SATURATION OF OXYGEN (SAO2)	SAO2	<92 %	0.200
	END TIDAL CO2	ETCO2	<35 OR >45	0.100
	FIO2	FIO2	>21 %	0.300
	PARTIAL PRESSURE OF CARBON DIOXIDE (PACO2)	PACO2	<35 OR >45	0.100
INFLAMMATION	TEMPERATURE	TEMP	<36 OR >38	0.400
	PULSE	HR	>90	0.100
	GLUCOSE	GLUCOSE	>125	0.100
	WHITE BLOOD CELL COUNT	WBC	<4,000 OR >12,000	0.400

Demographics. Demographic features remain constant throughout hospitalization. The examined data set contains both age and sex.

Here, the vital signs (regularly sampled) and raw Lab values (irregularly sampled) are exogenous variables, whereas SAD indicators are endogenous. The irregularly sampled series will be handled via forwarding filling. Our primary interest is to study all exogenous and endogenous series' effects on endogenous series and construct (Granger causal) graph/network over endogenous series.



2.2 Discrete Hawkes network

Model formulation. Suppose we observe N_1 sequences of binary SADs on time horizon T : $\{y_1^{(i)}, \dots, y_T^{(i)}\}$, $i = 1, \dots, N_1$; we also observe both continuous- and discrete-valued time series $\{x_1^{(i)}, \dots, x_T^{(i)}\}$, $i = 1, \dots, N_2$, which are vital signs and Lab test counts, and demographic variables (z_1, \dots, z_{N_3}) . In the following, we will call each of those SADs a node variable since it corresponds to a node in the Granger causal graph. With such a model at hand, we can better understand the dynamics within the human body, and most importantly, alert the clinicians to the potential causes and complications of an identified SAD.

To model the mutual excitation among those series, we propose a generalized linear model, which closely resembles the intensity function of Hawkes point process [Hawkes, 1971a,b, Hawkes and Oakes, 1974]. For i -th node variable ($i = 1, \dots, N_1$), at time step t ($t = 2, \dots, T$), we assume:

$$\mathbb{P} \left(y_t^{(i)} = 1 \mid \mathcal{H}_{t-1} \right) = g \left(\nu_i + \sum_{j=1}^{N_3} \gamma_{ij} z_j + \sum_{\tau=1}^{t-1} \sum_{j=1}^{N_2} \beta_{ij} x_{t-\tau}^{(j)} e^{-\tilde{R}_{ij}\tau} + \sum_{\tau=1}^{t-1} \sum_{j=1}^{N_1} \alpha_{ij} y_{t-\tau}^{(j)} e^{-R_{ij}\tau} \right), \quad (1)$$

where \mathcal{H}_t denotes the past observation up to time t and $g : \mathbb{R} \rightarrow [0, 1]$ is a link function. For example, g can be non-linear, such as sigmoid link function $g(x) = 1/(1 + e^{-x})$; also, it can be linear $g(x) = x$, which should be restricted on domain $[0, 1] \subset \mathbb{R}$.

Non-linear Granger causal graph. By the definition of Granger causality in non-linear model [Tank et al., 2018], we know that matrix $A = (\alpha_{ij}) \in \mathbb{R}^{N_1 \times N_1}$ represents the causal graph structure over N_1 SAD nodes. To be precise, we say j -th SAD does NOT Granger cause i -th SAD if $\alpha_{ij} = 0$.

Connection to Hawkes process. For i -th SAD node variable, α_{ij} and β_{ij} represent the magnitude of triggering effect of j -th SAD node variable and continuous variable to it. This effect decays exponentially fast with exponent characterized by R_{ij} and \tilde{R}_{ij} . γ_{ij} 's represent the influence of demographics and contribute to baseline intensity together with ν_i . Note that the above model

can be viewed as a discretized version of (non-linear) Hawkes process network with exponential triggering function [Wang et al., 2020]; other methods in learning Hawkes network include Xu et al. [2016], Achab et al. [2017], we do not dig deeper in this direction since it is out of the scope of this work.

3 Parameter estimation with variational inequality

In this section, we will leverage a recently developed technique [Juditsky and Nemirovski, 2019, Juditsky et al., 2020], which estimates the parameters of the generalized linear model by solving stochastic monotone variational inequality (VI), to develop a statistically principled method to estimate the parameters of discrete Hawkes network and infer the Granger causal graph topology.

Preliminaries. To begin with, we make reasonable simplification by assuming finite memory depth d for both continuous and binary observations. Let w_{t-d}^{t-1} denote the observation from $t-d$ to $t-1$:

$$\left(1, z_1, \dots, z_{N_3}, x_{t-1}^{(1)}, \dots, x_{t-d}^{(1)}, \dots, x_{t-1}^{(N_2)}, \dots, x_{t-d}^{(N_2)}, y_{t-1}^{(1)}, \dots, y_{t-d}^{(1)}, \dots, y_{t-1}^{(N_1)}, \dots, y_{t-d}^{(N_1)}\right)^{\top},$$

where superscript \top denotes matrix transpose. Since we only consider finite memory depth for binary observation, we could use one single parameter $\alpha_{ij\tau} := \alpha_{ij} \exp\{-R_{ij\tau}\}$ (similarly, $\beta_{ij\tau} := \beta_{ij} \exp\{-\tilde{R}_{ij\tau}\}$) to represent the triggering effect with exponential decay. We rewrite (1) into

$$\mathbb{P}\left(y_t^{(i)} = 1 \mid w_{t-d}^{t-1}\right) = g\left((w_{t-d}^{t-1})^{\top} \theta_i\right), \quad t = d+1, \dots, T, \quad i = 1, \dots, N_1, \quad (2)$$

where $\theta_i \in \mathbb{R}^N$ ($N = 1 + N_3 + dN_2 + dN_1$) is the parameter to be estimated:

$$\theta_i = (\nu_i, \gamma_{i1}, \dots, \gamma_{iN_3}, \beta_{i11}, \dots, \beta_{i1d}, \beta_{iN_21}, \dots, \beta_{iN_2d}, \alpha_{i11}, \dots, \alpha_{i1d}, \alpha_{iN_11}, \dots, \alpha_{iN_1d})^{\top}.$$

This parameter summarizes the influence from all variables to node i and could be estimated independently from the remaining $N_1 - 1$ parameters.

Granger Causality. We can see (2) is actually a generalized linear version of Vector Autoregressive (VAR) model. Therefore, we say j -th node series $\{y_t^{(j)}\}$ (or vital sign series $\{x_t^{(j)}\}$) Granger-causes i -th node series $\{y_t^{(i)}\}$ if $\alpha_{ij\tau} \neq 0$ (or $\beta_{ij\tau} \neq 0$) for some $\tau \in \{1, \dots, d\}$.

Estimation method. Denote the observation by $W_T := (w_{1-d}^0, \dots, w_{T-d+1}^T) \in \mathbb{R}^{(T+1) \times N}$, where variables observed at time step $1-d, \dots, 0$ are viewed as given history. We assume parameter θ_i is constrained in a convex compact set $\theta_i \in \Theta_i \subset \mathbb{R}^N$, then, for $i = 1, \dots, N_1$, we use the weak

solution to the following variational inequality as the estimator $\widehat{\theta}_i$:

$$\text{find } \widehat{\theta}_i \in \Theta_i : \langle F_{W_T}^{(i)}(\theta), \theta - \widehat{\theta}_i \rangle \geq 0, \quad \forall \theta \in \Theta_i, \quad \text{VI}[F_{W_T}^{(i)}, \Theta_i]$$

where $F_{W_T}^{(i)}(\theta_i)$ is the empirical vector field and defined as follows:

$$F_{W_T}^{(i)}(\theta_i) := \frac{1}{T} \sum_{t=1}^T w_{t-d}^{t-1} \left(g((w_{t-d}^{t-1})^\top \theta_i) - y_t^{(i)} \right).$$

Remarks. (i) The intuition behind this method is straightforward. Let's consider the global counterpart of the above vector field, whose root/weak solution is the unknown ground truth θ_i^{true} ,

$$F^{(i)}(\theta_i) := \mathbb{E}_{(w, y^{(i)})} [w (g(w^\top \theta_i) - y^{(i)})] = \mathbb{E}_{(w, y^{(i)})} [w (g(w^\top \theta_i) - g(w^\top \theta_i^{\text{true}}))].$$

Although we cannot access this global counterpart, by solving the empirical one $\text{VI}[F_{W_T}^{(i)}, \Theta_i]$ we could approximate the ground truth very well. We will show how well this approximation would be in the next section. (ii) Least Square Estimation for Linear VAR model and Maximum Likelihood Estimation for logistic regression model are both special cases of our proposed VI estimates; detailed derivations are deferred to Appendix B.1.

4 Non-asymptotic error bound and confidence interval

Now, we show the VI estimate will eventually converge to a very small neighborhood of the ground truth. Besides, we will derive a linear program (LP) based confidence interval (CI) of parameters θ_i 's.

Non-asymptotic bound on estimation error. To begin with, we state two necessary model assumptions:

Assumption 1. The link function $g(\cdot)$ is continuous and monotone, and the vector field $G(\theta) = \mathbb{E}_w [wg(w^\top \theta)]$ is well defined (and therefore monotone along with g). Moreover, g is differentiable and has uniformly bounded first order derivative $m_g \leq |g'| \leq M_g$ for positive constants m_g, M_g .

Assumption 2. The observations (static, binary and continuous) are bounded almost surely: there exists $M_w > 0$ such that at any time step t , we have $\|w_{t-d}^{t-1}\|_\infty \leq M_w$ with probability one.

We will use an auxiliary vector field defined as follows:

$$\tilde{F}_{W_T}^{(i)}(\theta_i) := \frac{1}{T} \sum_{t=1}^T w_{t-d}^{t-1} (g((w_{t-d}^{t-1})^\top \theta_i) - g((w_{t-d}^{t-1})^\top \theta_i^{\text{true}})).$$

This vector field changes the constant term in $F_{W_T}^{(i)}(\theta_i)$ to make sure its unique root/weak solution to corresponding VI is the unknown ground truth θ_i^{true} . Recall that $\hat{\theta}_i$ is the root of $F_{W_T}^{(i)}(\theta_i)$. Then, we will bound the difference between $\hat{\theta}_i$ and θ_i^{true} via the difference between $F_{W_T}^{(i)}(\theta_i)$ and $\tilde{F}_{W_T}^{(i)}(\theta_i)$:

$$\Delta^{(i)} := F_{W_T}^{(i)}(\theta_i) - \tilde{F}_{W_T}^{(i)}(\theta_i) = F_{W_T}^{(i)}(\theta_i^{\text{true}}).$$

Lemma 1. Under Assumptions 1 and 2, for $i = 1, \dots, N_1$, $\forall \varepsilon \in (0, 1)$, with probability at least $1 - \varepsilon$, the difference between the empirical and auxiliary vector field $\Delta^{(i)}$ can be bounded as follows:

$$\|\Delta^{(i)}\|_\infty \leq M_w \sqrt{\log(2N/\varepsilon)/T} \quad (3)$$

Moreover, this implies

$$\|\Delta^{(i)}\|_2 \leq M_w \sqrt{N \log(2N/\varepsilon)/T}. \quad (4)$$

The proof of the above lemma leverages the concentration property for martingales. Similar results could also be found in Juditsky et al. [2020], Wei et al. [2021]. We defer its proof to Appendix B.2. We want to remark that further improvement on this bound can be achieved by Bernstein inequality (as Juditsky et al. [2020] did), but the order will remain the same.

Theorem 1 (Upper bound on $\|\hat{\theta}_i - \theta_i^{\text{true}}\|_2$). Under Assumptions 1 and 2, for $i = 1, \dots, N_1$ and any $\varepsilon \in (0, 1)$, with probability at least $1 - \varepsilon$, the ℓ_2 distance between ground truth θ_i^{true} and $\hat{\theta}_i$, which is weak solution to $\text{VI}[F_{W_T}^{(i)}, \Theta_i]$, can be upper bounded as follows :

$$\|\hat{\theta}_i - \theta_i^{\text{true}}\|_2 \leq \frac{M_w}{m_g \lambda_1} \sqrt{\frac{N \log(2N/\varepsilon)}{T}},$$

where where λ_1 is the smallest eigenvalue of $\mathbb{W}_{1:T} = \sum_{t=1}^T w_{t-d}^{t-1} (w_{t-d}^{t-1})^\top / T$.

Remarks. (i) The above theorem is an extension to the general link function case of Theorem 1 [Juditsky et al., 2020], where they only sketched the proof without giving further details; we defer the detailed proof to Appendix B.2. (ii) As pointed out in Juditsky et al. [2020], $\mathbb{W}_{1:T} \in \mathbb{R}^{N \times N}$ will be full rank when T is sufficiently large, i.e., with high probability, λ_1 will be a positive constant.

Linear Program-based confidence interval. As pointed out in section II.E [Juditsky et al., 2020], for general non-linear link function g , it would be hard to separate θ_i from $\sum_{t=1}^T w_{t-d}^{t-1} g((w_{t-d}^{t-1})^\top \theta_i) / T$.

First, we derive a CI for linear link function case via a more precise data-driven bound for $F_{W_T}^{(i)}(\theta_i) \in \mathbb{R}^N$ as Juditsky et al. [2020] did in Lemma 2 (see its proof in Appendix B.3):

Proposition 1 (Confidence interval for linear transform of θ_i for linear link function case). Under Assumptions 1 and 2, for $i = 1, \dots, N_1$, and every $s > 1$, the following holds with probability at least $1 - 2N\{s[\log((s-1)T) + 2] + 2\}e^{1-s}$:

$$\theta_\ell[W_T, s; i] \leq a^\top \theta_i \leq \theta_u[W_T, s; i], \quad \forall a \in \mathbb{R}^N,$$

where $\theta_\ell[W_T, s; i]$ and $\theta_u[W_T, s; i]$ are defined in (7) and (8), respectively.

This CI is obtained by solving LPs (7) and (8). For general non-linear link function g , since it is typically constrained in a compact subset to satisfy Assumption 1 (see Example 4 in Appendix B.1), we can obtain linear bounds on the non-linear link function and then repeat the above techniques to obtain similar CI; details on this generalization can be found in Appendix B.3.

5 Real data experiments

In Experiment 1, nodes in the network are constructed by a clinician based on well-known, measurable, physiologic relationships in the human body. This expert-driven approach is subsequently compared to a purely data-driven model for identifying possible clusters of inpatient data in Experiment 2.

5.1 Exp. 1: network topology based on known physiologic relationships

Feature construction. As previously described, vital sign measurements were condensed into single features represented by summary statistics (i.e., maximum, minimum, mean) of the past 6 hours, creating a total of 12 distinct representations of a patient’s vital signs. A count of total Lab tests over the past 6 hours was used as a proxy for patient acuity and was also incorporated as a feature. SAD nodes were created by grouping all 34 Lab measurements into ten nodes (see Table 1) representative of common physiologic derangements seen in sepsis. Moreover, instead of constructing a sequence of binary variables for each node, we assigned a risk score at each time, indicating the severity of the SAD. However, when a variable (i.e., node) was used as the response during modeling, it was treated as binary by applying indicator function $\mathbf{1}_{\{y>0\}}$.

Sub-group analysis. To simplify model development, we carried out a sub-group analysis and excluded demographic features from the model. We used sex = 0 (female) and age > 60 sub-group

in the following to demonstrate our method, which contained 5,222 patients in the Physionet data set.

Model fitting. The primary outcome of interest was sepsis, which necessitated the addition of an 11-th binary time series called “SepsisLabel” to our data. This resulted in a total of $N_1 = 11$ nodes in our network. Using each of those N_1 variables as responses (recall that risk scores were binarized when used as a response) and the rest as features, we performed forward feature selection and fitted logistic regression models with hyperparameter being the number of training iterations.

The primary cross-validation criterion for both feature selection and hyperparameter tuning was the True Positive (TP) rate (classification accuracy for positive samples); we also compared classification error and AUC. TP rate was chosen because in a clinical setting, particularly as it pertains to sepsis, greater importance is placed on not missing the disease (i.e., maintaining a high sensitivity) as opposed to producing a false alert. We defer further details of the training procedure to Appendix C.1.

Results and interpretation. As previously discussed, nodes were created by a clinician to identify the distinct types of measurable, physiologic change that accompanies sepsis-related illness (i.e., SAD nodes); however, the clinician did not determine the relationship amongst the SAD nodes. Rather, these relationships were an output of model training. Both Table 2 and Figure 1 illustrate a compelling network of SAD nodes that follow closely with known and expected causal relationships in sepsis-related illness. For example, the finding that Diminished Cardiac Output strongly promotes sepsis events or that Shock strongly promotes Coagulopathy are well-appreciated relationships. The primary outcome of interest for this work was sepsis; still, as demonstrated in Table 2, the causal relationship between any node pair can be estimated, giving clinician users insight into the probability of observing subsequent SADs after sepsis.

Bootstrap confidence intervals. We also performed uncertainty quantification via bootstrap. We determined the existence of an edge in the network based on the 90% bootstrap confidence interval (CI), i.e., we assigned zero weight to that edge if the CI contains zero; otherwise, we used the median of the bootstrap samples as the weight. The resulting network topology is reported below in Figure 2. Meanwhile, we also used classification error as the CV criterion to infer the network topology in Figure 7. We applied hard thresholding on the network topology to improve legibility by only keeping directed edges whose absolute weights are greater than 0.15. For the complete network topology (without hard thresholding), one can see Figures 8 and 9 in Appendix C.2.

The networks in Figure 2 help to elucidate which relationships are most important in the network, which is an essential aspect of interpretability. The network with forward selection shows a high level of influence by the Diminished Cardiac Output and Shock nodes. This is not surprising as both

Table 2: Coefficients for discrete Hawkes network. For each node, from left to right, and from the first row to the second row, the order of feature follows the order in forwarding selection.

RENAL INJURY (TP RATE = 0.724)	OXYGEN CARRYING DYSFUNCTION 0.355	DIMINISHED CARDIAC OUTPUT 0.025	OXYGENATION DYSFUNCTION 0.086	SHOCK 0.097	INFLAMMATION 0.057
	COAGULOPATHY 0.067	CHOLESTASIS 0.179			
ELECTROLYTE IMBALANCE (TP RATE = 0.705)	OXYGEN CARRYING DYSFUNCTION 0.330	COAGULOPATHY 0.261	HR (MAX) 0.016	SEPSIS 0.065	OXYGENATION DYSFUNCTION 0.073
	INFLAMMATION 0.071				
OXYGEN CARRYING DYSFUNCTION (TP RATE = 0.703)	RENAL INJURY 0.287	COAGULOPATHY 0.431	ELECTROLYTE IMBALANCE 0.513	DIMINISHED CARDIAC OUTPUT 0.174	SHOCK -0.038
	OXYGENATION DYSFUNCTION 0.039	O2SAT MIN 0.139			
SHOCK (TP RATE = 0.673)	INFLAMMATION 0.088	DIMINISHED CARDIAC OUTPUT 0.234	HR (MAX) 0.324	COAGULOPATHY 0.350	RENAL INJURY 0.190
	ELECTROLYTE IMBALANCE 0.294	OXYGENATION DYSFUNCTION 0.148	ICULOS 0.097		
DIMINISHED CARDIAC OUTPUT (TP RATE = 0.622)	ELECTROLYTE IMBALANCE 0.086	SHOCK 0.117	INFLAMMATION 0.013	HEPATOCELLULAR INJURY 0.085	OXYGEN CARRYING DYSFUNCTION 0.233
	RESP MEAN -0.041	TEMP MAX 0.077			
COAGULOPATHY (TP RATE = 0.632)	HEPATOCELLULAR INJURY 0.173	OXYGEN CARRYING DYSFUNCTION 0.211	SHOCK 0.238	CHOLESTASIS 0.215	SEPSIS 0.019
	ELECTROLYTE IMBALANCE 0.259	RENAL INJURY 0.144	HR (MAX) 0.020		
CHOLESTASIS (TP RATE = 0.677)	SHOCK -0.002	HEPATOCELLULAR INJURY 0.864	HR (MEAN) 0.127	RENAL INJURY 0.295	COAGULOPATHY 0.397
	INFLAMMATION -0.002	SEPSIS 0.048	ICULOS 0.324	OXYGENATION DYSFUNCTION 0.089	
HEPATOCELLULAR INJURY (TP RATE = 0.619)	INFLAMMATION 0.060	OXYGEN CARRYING DYSFUNCTION 0.170	SHOCK 0.063	SEPSIS 0.088	DIMINISHED CARDIAC OUTPUT 0.043
	COAGULOPATHY 0.434	MAP (MIN) 0.063	O2SAT MIN 0.008	RENAL INJURY 0.262	
OXYGENATION DYSFUNCTION (TP RATE = 0.780)	SEPSIS 0.093	INFLAMMATION 0.047	RESP (MEAN) 2.538	SHOCK 0.699	DIMINISHED CARDIAC OUTPUT 0.237
	MAP MIN 0.060	HEPATOCELLULAR INJURY 0.111			
INFLAMMATION (TP RATE = 0.710)	SEPSIS 0.099	HR (MAX) 1.597	RENAL INJURY 0.117	OXYGENATION DYSFUNCTION 0.119	SHOCK 0.176
	HR (MEAN) 0.174	ICULOS 0.722	RENAL INJURY 0.509	INFLAMMATION 0.165	ELECTROLYTE IMBALANCE 0.200
SEPSIS (TP RATE = 0.768)	DIMINISHED CARDIAC OUTPUT 0.387	RESP (MIN) 0.458	COAGULOPATHY -0.104		

of these SADs are known to cause organ injury. The network that does not use forward selection has identified relationships that suggest certain SADs actually have an inhibitory effect. While there are possible explanations for these inhibitory effects, they are not commonly known or expected from a physiologic perspective. Overall, the network that employees forward feature selection demonstrates a more meaningful series of relationships consistent with known physiologic responses to sepsis.

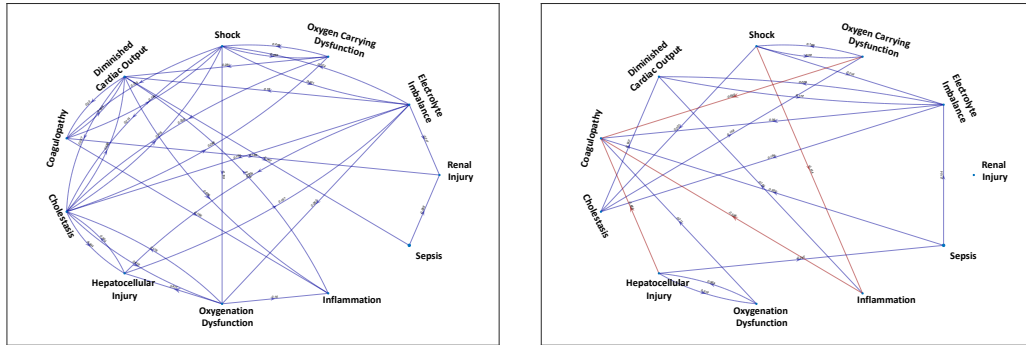


Figure 2: Bootstrap network topology with (left) and without (right) feature selection. We only keep (directed) edge with absolute weight greater than 0.15. The blue (directed) edge indicates a positive effect, whereas the red indicates a negative effect. The cross-validation criterion is TP rate.

5.2 Exp. 2: data-driven measurement clustering and network topology

In our second experiment, we assumed there was no prior information regarding the nature of the network and instead re-grouped the 34 measurements in Table 1 using a purely data-driven method. We constructed 34 binary time series and provided a label “1” if the Lab test was reported out AND the Lab result was abnormal based on the rules in Table 1.

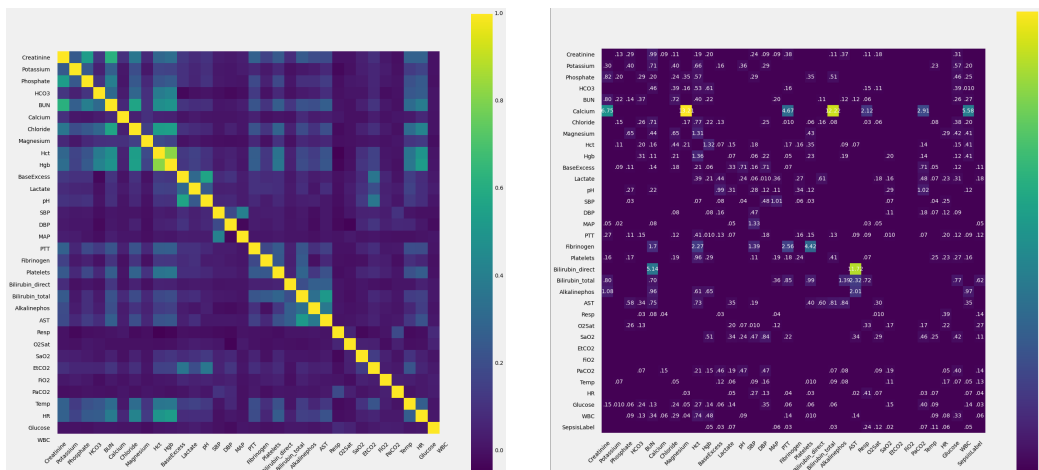


Figure 3: Correlation matrix (left) and adjacency matrix for discrete Hawkes network (right).

Hierarchical clustering based on “distance” matrix. Analysis of the similarity among measurements begins with the construction of a correlation matrix including all 34 measurements in Figure 3. In this case, correlation occurs when both variables are found to be abnormal. For example, one can see that when `Creatinine` is abnormal, it likely that `BUN` and `Phosphate` would also be abnormal based on the correlation matrix. This correlation and many of the others in the table like this are commonly found in sepsis patients.

We can view the correlation as statistical distance. Since larger correlation indicates smaller “distance”, we used the element-wise inverse of the correlation matrix as the distance matrix. Here we grouped those measurements based on positive correlation; for those with negative or zero correlation, we treated them as though they are very far away from each other and assigned a large constant as the distance. Then, we can apply (hierarchical) clustering to obtain the clusters. The resulting clusters are plotted in Figure 4.

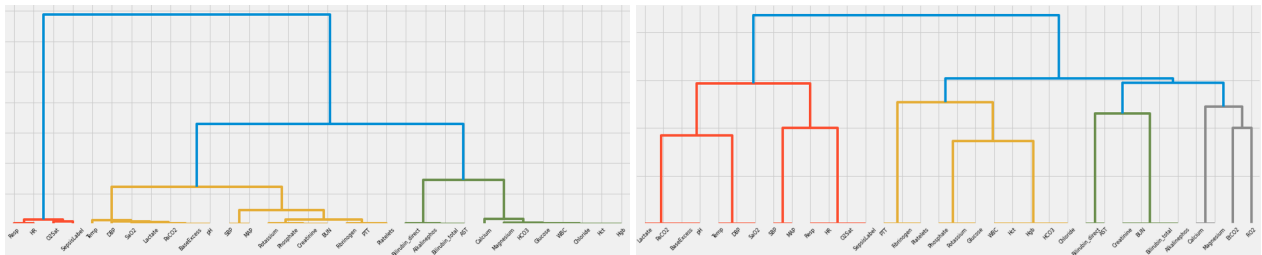


Figure 4: Hierarchical clustering based on correlation (left) and discrete Hawkes network (right).

Similar to the fitting procedure above, we fitted our proposed discrete Hawkes network model on those 34 binary time series to construct a directed graph. We plot the adjacency matrix in Figure 3. Here, the adjacency matrix is asymmetric, which makes it difficult to perform clustering. This asymmetric adjacency matrix A can be symmetrized by using $A_{sym} = A + A^T$. Then we can apply the same method as we did for the correlation matrix above to complete the (hierarchical) clustering. The result is plotted in Figure 4.

Both approaches for clustering patient features (i.e., via simple correlation and via a discrete Hawkes network) produce nodes that share similarity with the SAD nodes derived by a clinical expert in Experiment 1. For example, in Figure 4 we see a cluster that includes the measurements: `Lactate`, `PaCO2`, `BaseExcess`, `pH` which commonly become deranged during shock. While these measurements do occur together on a common Lab panel (i.e., they are often collected simultaneously), this doesn’t necessarily imply that their derangements would be similarly correlated as this label panel has many permutations of derangement caused by different non-sepsis disease processes. It is more reasonable to consider that the data-driven clustering methods are independently identifying clinically relevant SADs. While the simple correlation approach identifies concomitant

relationships (i.e., two things happening together), it does not consider a time-dependent, causal relationship the way the Hawkes network does. This important distinction is appreciated when considering the two maps in Figure 4. The Hawkes process develops nodes that have close intra-node relationships that are very clearly separated from other clusters. In contrast, the inter-node distances tend to be less pronounced in the correlation-based hierarchical clustering method.

Blockmodelling based on asymmetric Hawkes network. In this approach, we define clusters using a stochastic block model: for any two clusters V_i and V_j and any two nodes $a, b \in V_i$; then there is approximately the same number of in-edges (respectively out edges) connecting a to nodes in V_j and of in-edges (respectively out edges) connecting b to nodes in V_j . Identifying clusters from asymmetric adjacency matrix is called blockmodelling [Holland et al., 1983, Wang and Wong, 1987].

We introduce a spectral algorithm for blockmodelling [Sussman et al., 2012] in Appendix C.3. This algorithm has hyperparameters K (number of clusters/blocks) and d (top d eigenvectors are kept in the spectral decomposition). Since it only deals with unweighted directed graphs, we construct the unweighted adjacency matrix by thresholding with 0.15 as we did before. By applying the spectral algorithm recursively, we get hierarchical blockmodels and report the results in Figure 5.

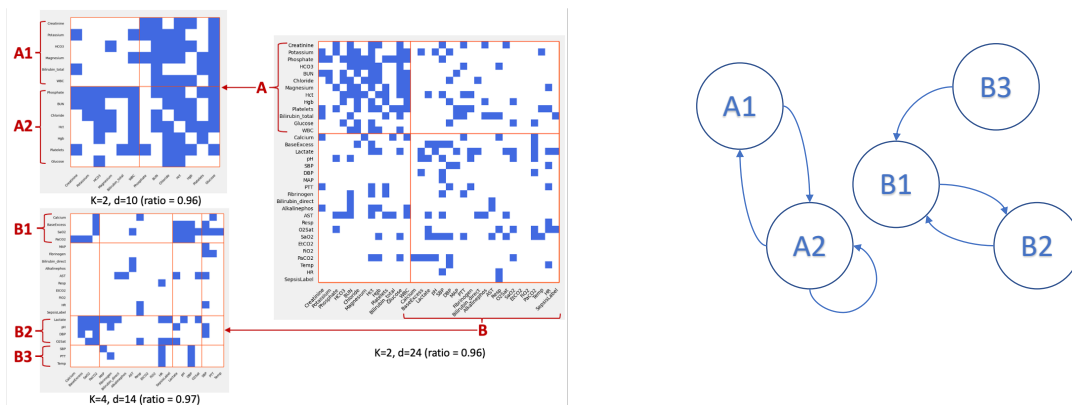


Figure 5: Left: Hierarchical Blockmodelling (hyperparameter under each plot). We chose the smallest d such that the explained variance ratio is at least 95%. Right: the resulting network topology.

Based on Hierarchical Blockmodelling, we identify five blocks/clusters and the associated network topology among them. Analysis of the first level suggests a predominantly renal-inflammatory axis in Group A with values like Creatinine, BUN, Phosphate, WBC being important, and a cardio-pulmonary axis in Group B with values like SaO2, O2Sat, SBP, Temp being important. Inside of Group A, we see derangements following known patterns that demonstrate renal injury (A1) promoting electrolyte imbalances (A2). Similarly, we see in Group B that reduced

blood pressure and fevers (B3) promote aberrations in oxygenation and acid/base equilibrium (B2) (a frequent association in sepsis). For demonstration purposes, this Hierarchical Blockmodel created the adjacency matrix using a threshold of 0.15; however, this could be lowered to identify a higher number of clusters and relationships. While single nodes are grouped together to form a cluster, it does not necessarily mean there is a correlation within the cluster (unless there is a self-directed edge (e.g., A2). Instead, the composite effect of nodes within a cluster promote dysfunction in the nodes of other clusters to which it is connected.

Table 3: Data-driven cluster based on Hierarchical Blockmodelling.

1ST-LEVEL CLUSTER	2ND-LEVEL CLUSTER	MEASUREMENT PHYSIONET NAME
A	A1	CREATININE , POTASSIUM , HCO3 , MAGNESIUM , BILIRUBIN TOTAL , WBC ;
	A2	PHOSPHATE , BUN , CHLORIDE , HCT , HGB , PLATELETS , GLUCOSE ;
B	B1	CALCIUM , BASEEXCESS , SAO2 , PACO2 ;
	B2	LACTATE , PH , DBP , O2SAT ;
	B3	SBP , PTT , TEMP ;
	NA	MAP , FIBRINOGEN , BILIRUBIN DIRECT , ALKALINEPHOS , AST , RESP , ETCO2 , FIO2 , HR , SEPSISLABEL

6 Discussion

We develop a model to infer non-linear Granger causality from mixed-type of irregularly sampled time-series, and leverage a recently developed stochastic variational inequality (VI) approach to estimate the model parameters. We conduct a non-asymptotic theoretical analysis and demonstrate the good performance of our proposed method coupled with heuristic forward feature selection via real data experiments. Future work includes connecting this newly developed VI approach with a principled subsection selection method (e.g., group Lasso). It is important to appreciate that many of the Lab tests that serve as a data source for our analysis are collected at the direction of a clinician, meaning there is an inherent component of suspicion associated with each Lab test. The important effects that drive suspicion and compel the ordering of tests may not be captured in our data and, subsequently, our network. Additionally, our cohort was limited to a specific subset of patients in order to reduce the number of data elements and make analysis more tractable, but it is commonly recognized that there are demographic features and co-existing medical conditions that affect how patients respond to sepsis. These unobserved features may also alter some of the findings for our network. It is also important to appreciate that we accepted the consequence of increased false alarms (i.e. False Positives) in order to maximize our sensitivity. In clinical settings high false alarm rates may decrease clinical satisfaction and lead to alarm fatigue or disuse.

In summary, our experimental results serve as a demonstration that good performance is achievable with our proposed method. The development of a full, interpretable, causal graph capable of facilitating real-world clinical decision-making would require the analysis of a larger cohort of patients from multiple health systems with a more robust set of demographic data. An interpretable model like the one we have proposed offers some protection against the aforementioned limitations by allowing a clinician to combine their own knowledge about a patient with the findings of the model resulting in more informed decisions about a patient's health status.

References

- ABIM. American board of internal medicine: Laboratory reference ranges. URL <https://www.abim.org/Media/bfijryql/laboratory-reference-ranges.pdf>.
- Massil Achab, Emmanuel Bacry, Stéphane Gaïffas, Iacopo Mastromatteo, and Jean-François Muzy. Uncovering causality from multivariate Hawkes integrated cumulants. In *International Conference on Machine Learning*, pages 1–10. PMLR, 2017.
- Sumanta Basu, Ali Shojaie, and George Michailidis. Network Granger causality with inherent grouping structure. *The Journal of Machine Learning Research*, 16(1):417–453, 2015.
- Sumanta Basu, Xianqi Li, and George Michailidis. Low rank and structured modeling of high-dimensional vector autoregressions. *IEEE Transactions on Signal Processing*, 67(5):1207–1222, 2019.
- Andrew Bolstad, Barry D Van Veen, and Robert Nowak. Causal network inference via group sparse regularization. *IEEE transactions on signal processing*, 59(6):2628–2641, 2011.
- John Anda Du, Nadi Sadr, and Philip de Chazal. Automated prediction of sepsis onset using gradient boosted decision trees. In *2019 Computing in Cardiology (CinC)*, pages Page–1. IEEE, 2019.
- Lucas M Fleuren, Thomas LT Klausch, Charlotte L Zwager, Linda J Schoonmade, Tingjie Guo, Luca F Roggeveen, Eleonora L Swart, Armand RJ Girbes, Patrick Thorat, Ari Ercole, et al. Machine learning for the prediction of sepsis: a systematic review and meta-analysis of diagnostic test accuracy. *Intensive care medicine*, 46(3):383–400, 2020.
- Alan G Hawkes. Point spectra of some mutually exciting point processes. *Journal of the Royal Statistical Society: Series B (Methodological)*, 33(3):438–443, 1971a.
- Alan G Hawkes. Spectra of some self-exciting and mutually exciting point processes. *Biometrika*, 58(1):83–90, 1971b.
- Alan G Hawkes and David Oakes. A cluster process representation of a self-exciting process. *Journal of Applied Probability*, 11(3):493–503, 1974.
- Paul W Holland, Kathryn Blackmond Laskey, and Samuel Leinhardt. Stochastic blockmodels: First steps. *Social networks*, 5(2):109–137, 1983.
- Anatoli Juditsky, Arkadi Nemirovski, Liyan Xie, and Yao Xie. Convex parameter recovery for interacting marked processes. *IEEE Journal on Selected Areas in Information Theory*, 2020.

- Anatoli B Juditsky and AS Nemirovski. Signal recovery by stochastic optimization. *Automation and Remote Control*, 80(10):1878–1893, 2019.
- Helmut Lütkepohl. *New introduction to multiple time series analysis*. Springer Science & Business Media, 2005.
- William B Nicholson, David S Matteson, and Jacob Bien. Varx-l: Structured regularization for large vector autoregressions with exogenous variables. *International Journal of Forecasting*, 33(3):627–651, 2017.
- M. A. Reyna, C. S. Josef, R. Jeter, S. P. Shashikumar, M. B. Westover, S. Nemati, G. D. Clifford, and A. Sharma. Early Prediction of Sepsis From Clinical Data: The PhysioNet/Computing in Cardiology Challenge 2019. *Crit Care Med*, 48(2):210–217, 02 2020.
- Matthew A Reyna, Chris Josef, Salman Seyedi, Russell Jeter, Supreeth P Shashikumar, M Brandon Westover, Ashish Sharma, Shamim Nemati, and Gari D Clifford. Early prediction of sepsis from clinical data: the physionet/computing in cardiology challenge 2019. In *2019 Computing in Cardiology (CinC)*, pages Page–1. IEEE, 2019.
- Christopher W. Seymour, Foster Gesten, Hallie C. Prescott, Marcus E. Friedrich, Theodore J. Iwashyna, Gary S. Phillips, Stanley Lemeshow, Tiffany Osborn, Kathleen M. Terry, and Mitchell M. Levy. Time to Treatment and Mortality during Mandated Emergency Care for Sepsis. *N. Engl. J. Med.*, 376(23):2235–2244, 2017. ISSN 1533-4406. doi: 10.1056/NEJMoa1703058.
- Supreeth P. Shashikumar, Christopher S. Josef, Ashish Sharma, and Shamim Nemati. DeepAISE – An interpretable and recurrent neural survival model for early prediction of sepsis. *Artificial Intelligence in Medicine*, 113:102036, March 2021. ISSN 0933-3657. doi: 10.1016/j.artmed.2021.102036. URL <https://www.sciencedirect.com/science/article/pii/S0933365721000294>.
- Ali Shojaie and Emily B Fox. Granger causality: A review and recent advances. *arXiv preprint arXiv:2105.02675*, 2021.
- Vikas Sindhvani, Minh Ha Quang, and Aurélie C Lozano. Scalable matrix-valued kernel learning for high-dimensional nonlinear multivariate regression and granger causality. *arXiv preprint arXiv:1210.4792*, 2012.
- Mervyn Singer, Clifford S Deutschman, Christopher Warren Seymour, Manu Shankar-Hari, Djillali Annane, Michael Bauer, Rinaldo Bellomo, Gordon R Bernard, Jean-Daniel Chiche, Craig M

- Coopersmith, et al. The third international consensus definitions for sepsis and septic shock (sepsis-3). *Jama*, 315(8):801–810, 2016.
- Daniel L Sussman, Minh Tang, Donniell E Fishkind, and Carey E Priebe. A consistent adjacency spectral embedding for stochastic blockmodel graphs. *Journal of the American Statistical Association*, 107(499):1119–1128, 2012.
- Alex Tank, Ian Covert, Nicholas Foti, Ali Shojaie, and Emily Fox. Neural granger causality for nonlinear time series. *stat*, 1050:16, 2018.
- Hadrien Van Lierde, Jean-Charles Delvenne, Paul Van Dooren, and Marco Saerens. Spectral clustering algorithms for directed graphs, 2015.
- Haoyun Wang, Liyan Xie, Alex Cuzzo, Simon Mak, and Yao Xie. Uncertainty quantification for inferring hawkes networks. *arXiv preprint arXiv:2006.07506*, 2020.
- Yuchung J Wang and George Y Wong. Stochastic blockmodels for directed graphs. *Journal of the American Statistical Association*, 82(397):8–19, 1987.
- Song Wei, Yao Xie, and Dobromir Rahnev. Inferring serial correlation with dynamic backgrounds. *arXiv preprint arXiv:2101.10962*, 2021.
- WHO. Global report on the epidemiology and burden of sepsis: current evidence, identifying gaps and future directions. 2020.
- Hongteng Xu, Mehrdad Farajtabar, and Hongyuan Zha. Learning granger causality for hawkes processes. In *International Conference on Machine Learning*, pages 1717–1726. PMLR, 2016.
- Meicheng Yang, Chengyu Liu, Xingyao Wang, Yuwen Li, Hongxiang Gao, Xing Liu, and Jianqing Li. An explainable artificial intelligence predictor for early detection of sepsis. *Critical Care Medicine*, 48(11):e1091–e1096, 2020.
- Morteza Zabihi, Serkan Kiranyaz, and Moncef Gabbouj. Sepsis prediction in intensive care unit using ensemble of xgboost models. In *2019 Computing in Cardiology (CinC)*, pages Page–1. IEEE, 2019.

A Inference with least square estimation

One of the most commonly used methods in statistics and machine learning for parameter estimation is least square estimation (LSE). This conceptually simple approach allows one to estimate parameters by minimizing the least square objective as follows:

$$\min_{\Gamma, A, B, R, \tilde{R}} f(\Gamma, A, B, R, \tilde{R}; \mathcal{H}_T) := \sum_{t=d+1}^T \sum_{i=1}^N \left(y_t^{(i)} - \mathbb{P} \left(y_t^{(i)} = 1 \mid \mathcal{H}_{t-1} \right) \right)^2. \quad (5)$$

However, this conceptual simplicity comes at the price of more stringent model assumptions. For example, it is typically desired to have a convex optimization problem, which requires careful selection of link function.

Proposition 2. A sufficient condition for the optimization problem (5) to be convex is that the link function $g(x)$ is concave.

For general link function, e.g., sigmoid link function, the concavity cannot be satisfied and therefore optimization problem (5) will be non-convex. Nevertheless, we could apply stochastic gradient descent (SGD) to solve this non-convex optimization problem. Assume we have multiple observations over the network: $Y_m = \{y_t^{(i)}(m)\}_{i=1, \dots, N_1, t=1, \dots, T_m}$, $X_m = \{x_t^{(i)}(m)\}_{i=1, \dots, N_2, t=1, \dots, T_m}$, $Z_m = \{z_i(m)\}_{i=1, \dots, N_3}$, $m = 1, \dots, M$. Note that we could decouple the original optimization problem (5) into N_1 sub-problems since the objective can be split into

$$f(\Gamma, A, B, R, \tilde{R}; \mathcal{H}_T) = \sum_{i=1}^N \sum_{t=1}^T \left(y_t^{(i)} - \mathbb{P} \left(y_t^{(i)} = 1 \mid \mathcal{H}_t \right) \right)^2 := \sum_{i=1}^N f_i(\Gamma_i, A_i, B_i, R_i, \tilde{R}_i; \mathcal{H}_T),$$

where the subscript i means we fix the first index to be i — we are studying how other nodes influence node i . Then the vanilla SGD algorithm is as follows:

Algorithm 1 Vanilla SGD

Input: choose stopping critical value ε (e.g., 10^{-2}), step size η (e.g., 5×10^{-3}), maximum number of iterations n and iteration number index $j = 0$.

Initialize: arbitrarily initialize $\Gamma^{(0)}, A^{(0)}, B^{(0)}, R^{(0)}, \tilde{R}^{(0)}$, e.g., matrices of all zero entries, $f^{(-1)} = \infty$ and $f^{(0)} = \sum_{m=1}^k f(\Gamma^{(0)}, A^{(0)}, B^{(0)}, R^{(0)}, \tilde{R}^{(0)}; \mathcal{H}_{T_m})$.

while $|f^{(j-1)} - f^{(j)}| > \varepsilon$ and $j \leq n$ **do**

 Randomly select (a batch) of observations: $\mathcal{H}_{T_1} = (Y_1, X_1), \dots, \mathcal{H}_{T_k} = (Y_k, X_k)$.

for $i \in \{1, 2, \dots, N_1\}$ **do**

for scalar parameter v in $\Gamma_i^{(j)}, A_i^{(j)}, B_i^{(j)}, R_i^{(j)}, \tilde{R}^{(j)}$ **do**

$$v^{(j+1)} \leftarrow v^{(j)} - \eta \times \sum_{m=1}^k \nabla_v f_i(\Gamma^{(j)}, A^{(j)}, B^{(j)}, R^{(j)}, \tilde{R}^{(j)}; \mathcal{H}_{T_m})$$

end for

end for

$f^{(\ell)} = \sum_{m=1}^k f(\Gamma^{(\ell)}, A^{(\ell)}, B^{(\ell)}, R^{(\ell)}, \tilde{R}^{(\ell)}; \mathcal{H}_{T_m})$, for $\ell = j$ and $j + 1$.

$j \leftarrow j + 1$.

end while

The above algorithm is the general procedure for SGD. However, we should make a few modifications in order to adapt to our setting:

1. Due to the non-convexity, there is no guarantee that the objective function is minimized at the ground truth. Furthermore, since our final objective is sepsis prediction, we use last time step prediction accuracy of sepsis label to form the stopping rule. Examples of metric of prediction accuracy include:

Example 1 (Least square loss). The least square loss function is

$$\ell_{LS}(\Gamma, A, B, R, \tilde{R}; \mathcal{H}_T) = \left(y_T^{sepsis} - \mathbb{P} \left(y_T^{sepsis} = 1 \mid \mathcal{H}_T \right) \right)^2.$$

Example 2 (0 – 1 loss). If we choose a threshold p , then the 0 – 1 loss function is

$$\ell_{0-1}(\Gamma, A, B, R, \tilde{R}; \mathcal{H}_T) = \left| y_T^{sepsis} - \mathbf{1} \left\{ \mathbb{P} \left(y_T^{sepsis} = 1 \mid \mathcal{H}_T \right) \geq p \right\} \right|.$$

2. To make sure the fitted model generalizes well, we use out-of-sample prediction accuracy. To be precise, we split the data we have into training and test data set. We still run the iterations as suggested in Algorithm 1 using training data, but only updates our final results when the prediction accuracy on the test data is improved.

3. To make the learning task easier, we use subgroup analysis to deal with the influence of demographic/static variables instead of learning them from SGD. To be precise, we split the data into subgroups based on demographic variables z . In this way, we could remove the variable Γ in the learning process. Here, we fix $\Gamma = 0$ and do not update it in the SGD. In the following, we will simply omit Γ .

By taking the above three modifications into account, we have the modified SGD as shown in Algorithm 2.

Algorithm 2 Modified SGD

Input: Training data $\mathcal{H}_{T_i} = (Y_i, X_i, Z_i), i = 1, \dots, K$ test data $\mathcal{H}_{T_i} = (Y_i, X_i, Z_i), i = K + 1, \dots, K + k$. Choose stopping critical value ε (e.g., 10^{-2}), step size η (e.g., 5×10^{-3}), maximum number of iterations n and iteration number index $j = 0$.

Initialize: arbitrarily initialize $A^{(0)}, B^{(0)}, R^{(0)}$, e.g., matrices of all zero entries, $\ell^{(-1)} = \infty$ and $\ell^{(0)} = \sum_{m=1}^k \ell(A^{(0)}, B^{(0)}, R^{(0)}, \tilde{R}^{(0)}; \mathcal{H}_{T_{m+K}})$. Let $A, B, R = A^{(0)}, B^{(0)}, R^{(0)}, \tilde{R}^{(0)}$.

while $|\ell^{(j-1)} - \ell^{(j)}| > \varepsilon$ and $j \leq n$ **do**

Randomly select (a batch of) M observations from training data: $\mathcal{H}_{T_{i_m}} = (Y_{i_m}, X_{i_m}, Z_{i_m}), 1 < i_1 < \dots < i_M < K$.

for $i \in \{1, 2, \dots, N_1\}$ **do**

for scalar parameter v in $A_i^{(j)}, B_i^{(j)}, R_i^{(j)}, \tilde{R}^{(j)}$ **do**

$$v^{(j+1)} \leftarrow v^{(j)} - \eta \times \sum_{m=1}^M \nabla_v f_{i_m}(A^{(j)}, B^{(j)}, R^{(j)}, \tilde{R}^{(j)}; \mathcal{H}_{T_{i_m}}).$$

end for

end for

Evaluate the out-of-sample prediction accuracy at the updated parameters:

$$\ell^{(j+1)} = \sum_{m=1}^k \ell(A^{(j+1)}, B^{(j+1)}, R^{(j+1)}, \tilde{R}^{(j+1)}; \mathcal{H}_{T_{m+K}}).$$

if $\ell^{(j+1)} < \ell^{(j)}$ **then**

$$A, B, R \leftarrow A^{(j+1)}, B^{(j+1)}, R^{(j+1)}, \tilde{R}^{(j+1)}.$$

end if

$$j \leftarrow j + 1.$$

end while

Output: A, B, R .

B Technical details

B.1 Two special cases

Example 3 (Linear link function). Here, we consider a special case where $g(x) = x$. To make sure the model (2) indeed returns a meaningful probability, we constrain the parameter θ_i to take value in $\Theta_i := \{\theta_i : 0 \leq (w_{t-d}^{t-1})^\top \theta_i \leq 1, t = 1, \dots, T\}$. In this special case, the vector field becomes

$$F_{W_T}^{(i)}(\theta_i) = \frac{1}{T} \sum_{t=1}^T w_{t-d}^{t-1} (w_{t-d}^{t-1})^\top \theta_i - \frac{1}{T} \sum_{t=1}^T w_{t-d}^{t-1} y_t^{(i)} := \mathbb{W}_{1:T} \theta_i - \frac{1}{T} \sum_{t=1}^T w_{t-d}^{t-1} y_t^{(i)},$$

where $\mathbb{W}_{1:T} := \sum_{t=1}^T w_{t-d}^{t-1} (w_{t-d}^{t-1})^\top / T \in \mathbb{R}^{N \times N}$. Moreover, this vector field is indeed the gradient field of least square objective and therefore the weak solution to the corresponding VI is the least square estimation (LSE):

$$\begin{aligned} & \underset{\theta_i}{\text{minimize}} && \frac{1}{2T} \sum_{t=1}^T \left(y_t^{(i)} - (w_{t-d}^{t-1})^\top \theta_i \right)^2 \\ & \text{subject to} && \theta_i \in \Theta_i = \{\theta_i : 0 \leq (w_{t-d}^{t-1})^\top \theta_i \leq 1, t = 1, \dots, T\}. \end{aligned} \quad (6)$$

We should remark the equivalence between our proposed VI estimate and LSE will only hold for linear link function, since the gradient field of LSE with general link function will be:

$$\frac{1}{T} \sum_{t=1}^T w_{t-d}^{t-1} g' \left((w_{t-d}^{t-1})^\top \theta_i \right) \left(g \left((w_{t-d}^{t-1})^\top \theta_i \right) - y_t^{(i)} \right).$$

Example 4 (Logistic regression). Another example is logistic regression, where the link function is $g(x) = (1 + e^{-x})^{-1}$. We can show that it is the gradient field of the objective of the following optimization problem:

$$\underset{\theta_i}{\text{minimize}} \quad -\frac{1}{T} \sum_{t=1}^T y_t^{(i)} \log g \left((w_{t-d}^{t-1})^\top \theta_i \right) + (1 - y_t^{(i)}) \log \left(1 - g \left((w_{t-d}^{t-1})^\top \theta_i \right) \right).$$

That is, VI estimate is the Maximum Likelihood estimator. This equivalence between VI estimate and MLE comes from the fact that $g'(x) = g(x)(1 - g(x))$.

To make sure Assumption 1 holds, we could constrain the parameter θ_i to take value in

$$\Theta_i := \{\theta_i : -M \leq (w_{t-d}^{t-1})^\top \theta_i \leq M, t = 1, \dots, T\}.$$

In this way, the first order derivative is bounded for any finite $M > 0$. Besides, by choosing

large enough M , it is reasonable to assume that the unknown true probability will stay in our constrained space. Moreover, the second assumption is mild, since for any collection of (sub-)Gaussian random variables, its largest value will be bounded with some positive constant with overwhelming probability. Then we could carry out our analysis below conditioning on that high probability event.

B.2 Proof of Theorem 1

Proof of Lemma 1. Denote random vector

$$\xi_t := w_{t-d}^{t-1} \left(g \left((w_{t-d}^{t-1})^\top \theta_i^{\text{true}} \right) - y_t^{(i)} \right).$$

Then we can re-write $\Delta^{(i)} = \sum_{t=1}^T \xi_t / T$. Define σ -field $\mathcal{F}_t := \sigma(W_t)$, and $\mathcal{F}_0 \subset \mathcal{F}_1 \subset \dots \subset \mathcal{F}_T$ form a filtration. It is easy to show

$$\mathbb{E}[\xi_t | \mathcal{F}_{t-1}] = 0, \quad \text{Var}(\xi_t | \mathcal{F}_{t-1}) = g \left((w_{t-d}^{t-1})^\top \theta_i \right) \left(1 - g \left((w_{t-d}^{t-1})^\top \theta_i \right) \right) \leq 1/4.$$

This means ξ_t ($t = 1, \dots, T$) is a Martingale Difference Sequence. Moreover, its infinity norm is bounded by M_w almost surely (Assumption 2). Therefore, by Azuma's inequality, we have

$$\mathbb{P} \left(|\Delta_k^{(i)}| > u \right) \leq 2 \exp \left\{ -\frac{u^2}{2TM_w^2} \right\}, \quad k = 1, \dots, N, \quad \forall u > 0,$$

where $\Delta_k^{(i)}$ is the k -th entry of vector $\Delta^{(i)}$. By union bound, we have

$$\mathbb{P} \left(|\Delta_k^{(i)}| > u, \quad k = 1, \dots, N \right) \leq 2N \exp \left\{ -\frac{u^2}{2TM_w^2} \right\}, \quad \forall u > 0.$$

By setting the RHS of above inequality to ε and solving for u , we prove (3). Besides, since $\|\Delta\|_2 \leq \sqrt{N} \|\Delta\|_\infty$ holds for any vector $\Delta \in \mathbb{R}^N$, we can easily prove (4) using (3). \square

Lemma 2 (Lemma 3.1 [Juditsky and Nemirovski, 2019]). Let Θ be a convex compact set and H be a monotone vector field on Θ with monotonicity modulus $\kappa > 0$, i.e.,

$$\forall z, z' \in \Theta, [H(z) - H(z')]^\top (z - z') \geq \kappa \|z - z'\|_2^2.$$

Then, the weak solution \bar{z} to $\text{VI}[H, \Theta]$ exists and is unique. It satisfies:

$$H(z)^\top (z - \bar{z}) \geq \kappa \|z - \bar{z}\|_2^2.$$

Lemma 3 (Property I of vector fields [Juditsky and Nemirovski, 2019]). Under Assumption 1, the vector field $F_{W_T}^{(i)}(\theta_i)$ is monotone modulus $m_g \lambda_1$, where λ_1 is the smallest eigenvalue of $\mathbb{W}_{1:T} = \sum_{t=1}^T w_{t-d}^{t-1} (w_{t-d}^{t-1})^\top / T$.

Proof of Lemma 3.

$$\begin{aligned}
\left(F_{W_T}^{(i)}(\theta) - F_{W_T}^{(i)}(\theta')\right)^\top (\theta - \theta') &= \frac{1}{T} \sum_{t=1}^T \left((w_{t-d}^{t-1})^\top \theta - (w_{t-d}^{t-1})^\top \theta' \right) \left(g \left((w_{t-d}^{t-1})^\top \theta \right) - g \left((w_{t-d}^{t-1})^\top \theta' \right) \right) \\
&\geq m_g \frac{1}{T} \sum_{t=1}^T \left\| (w_{t-d}^{t-1})^\top (\theta - \theta') \right\|_2^2 \\
&= m_g (\theta - \theta')^\top \frac{1}{T} \sum_{t=1}^T w_{t-d}^{t-1} (w_{t-d}^{t-1})^\top (\theta - \theta') \\
&\geq m_g \lambda_1 \|\theta - \theta'\|_2^2.
\end{aligned}$$

□

Proof of Theorem 1. By Lemma 3, we know that

$$\Delta_i^\top (\hat{\theta}_i - \theta_i^{\text{true}}) = \left(F_{W_T}^{(i)}(\hat{\theta}_i) - F_{W_T}^{(i)}(\theta_i^{\text{true}}) \right)^\top (\hat{\theta}_i - \theta_i^{\text{true}}) \geq m_g \lambda_1 \|\hat{\theta}_i - \theta_i^{\text{true}}\|_2^2.$$

By triangle inequality, we also have $\Delta_i^\top (\hat{\theta}_i - \theta_i^{\text{true}}) \leq \|\Delta_i\|_2 \|\hat{\theta}_i - \theta_i^{\text{true}}\|_2$. Together with (4) in Lemma 1, we complete the proof. □

B.3 Confidence interval

Proof of Proposition 1. We first define some notations:

$$\theta_\ell[W_T, s; i] = \min \left\{ \begin{array}{l} a^\top \theta_i : \theta_i \in \Theta_i, \\ \psi_\ell(a[W_T; i], T; s) \leq \frac{(\mathbb{W}_{1:T} \theta_i)_k}{M_w} \leq \psi_u(a[W_T; i], T; s), k = 1, \dots, N_1. \end{array} \right\} \quad (7)$$

$$\theta_u[W_T, s; i] = \max \left\{ \begin{array}{l} a^\top \theta_i : \theta_i \in \Theta_i, \\ \psi_\ell(a[W_T; i], T; s) \leq \frac{(\mathbb{W}_{1:T} \theta_i)_k}{M_w} \leq \psi_u(a[W_T; i], T; s), k = 1, \dots, N_1. \end{array} \right\} \quad (8)$$

Here,

$$\psi_\ell(\nu, N; y) = \begin{cases} (N + 2y)^{-1} \left[N\nu + \frac{2u}{3} - \sqrt{2N\nu y + \frac{y^2}{3} - \frac{2u}{N} \left(\frac{y}{3} - \nu N \right)^2} \right] & \text{if } \nu > \frac{y}{3N} \\ 0 & \text{otherwise} \end{cases}$$

$$\psi_u(\nu, N; y) = \begin{cases} (N + 2y)^{-1} \left[N\nu + \frac{4y}{3} + \sqrt{2N\nu y + \frac{5y^2}{3} - \frac{2y}{N} \left(\frac{y}{3} + \nu N \right)^2} \right] & \text{if } \nu < 1 - \frac{y}{3N} \\ 1 & \text{otherwise} \end{cases}$$

For $i = 1, \dots, N_1$, we will derive a more precise data-driven bound for $F_{W_T}^{(i)}(\theta_i) \in \mathbb{R}^N$ as Juditsky et al. [2020] did in Lemma 2:

Lemma 4. Under Assumptions 1 and 2, for $i = 1, \dots, N_1$, and every $s > 1$, the following holds with probability at least $1 - 2N\{s[\log((s-1)T) + 2] + 2\}e^{1-s}$:

$$M_w \psi_\ell(a[W_T; i], T; s) \mathbf{1}_N - a[W_T; i] \leq F_{W_T}^{(i)}(\theta_i) \leq M_w \psi_u(a[W_T; i], T; s) \mathbf{1}_N - a[W_T; i],$$

where $\mathbf{1}_N \in \mathbb{R}^N$ is the vector of ones, the inequality between vectors is element-wise and

$$a[W_T; i] := \sum_{t=1}^T w_{t-d}^{t-1} y_t^{(i)} / T.$$

Then, it is easy to complete the proof, since by the above Lemma, θ_i is a feasible solution to the linear programs (7) and (8) with probability at least $1 - 2N\{s[\log((s-1)T) + 2] + 2\}e^{1-s}$. \square

Proof of Lemma 4. Similar to the proof of Lemma 2 [Juditsky et al., 2020], we will make use of Lemma 4 therein to prove our Lemma 4 here.

We choose γ_t to be the k -th entry ($k = 1, \dots, N$) of w_{t-d}^{t-1} normalized by M_w such that it stays within $[0, 1]$, i.e. $\gamma_i = (w_{t-d}^{t-1})_k / M_w$. μ_t would be $g((w_{t-d}^{t-1})^\top \theta_i)$ and ν_t is the k -th entry of $a[W_T; i]$ normalized by M_w , i.e. $\nu_t := a[W_T; i]_k / M_w = \gamma_t y_t^{(i)}$. Then, by Lemma 4 [Juditsky et al., 2020], we complete the proof. \square

As for the general monotone non-linear link function, Lemma 4 still holds, but the vector field is no longer a linear transform of the coefficient vector. Nevertheless, θ_i would still be a feasible solution to the following optimization problem with high probability:

$$\theta_\ell[W_T, s; i] = \min \left\{ \begin{array}{l} a^\top \theta_i : \theta_i \in \Theta_i, \\ \psi_\ell(a[W_T; i], T; s) \leq \frac{1}{TM_w} \sum_{t=1}^T (w_{t-d}^{t-1})_k g((w_{t-d}^{t-1})^\top \theta_i) \\ \leq \psi_u(a[W_T; i], T; s), k = 1, \dots, N_1. \end{array} \right\} \quad (9)$$

$$\theta_u[W_T, s; i] = \max \left\{ \begin{array}{l} a^\top \theta_i : \theta_i \in \Theta_i, \\ \psi_\ell(a[W_T; i], T; s) \leq \frac{1}{TM_w} \sum_{t=1}^T (w_{t-d}^{t-1})_k g((w_{t-d}^{t-1})^\top \theta_i) \\ \leq \psi_u(a[W_T; i], T; s), k = 1, \dots, N_1. \end{array} \right\} \quad (10)$$

However, even by assuming g to be convex or concave, we cannot say the above optimization is convex. So direct generalization may be problematic. Nevertheless, we could use linear bounds on the nonlinear link function such that we can still get a LP. Again, we take logistic regression as an example, where the link function is sigmoid function $g(t) = \text{sig}(t) = \frac{1}{1+e^{-t}}$:

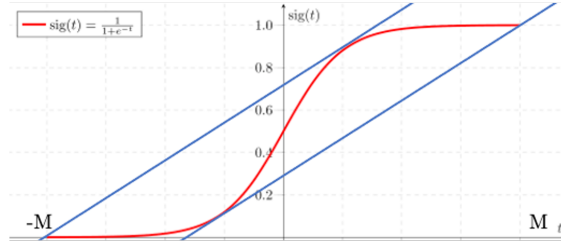


Figure 6: Illustration of linear bounds (blue lines) of the non-linear link function (red line).

Let the upper and lower linear bound be $f_1(x) = a_1x + b_1$ and $f_2(x) = a_2x + b_2$, respectively. we have $-a_1M + b_1 = 1/(1 + 1 + e^M)$ and $-a_1(\log(1 + \sqrt{1 - 4a_1}) - \log(1 - \sqrt{1 - 4a_1})) + b_1 = (1 + \sqrt{1 - 4a_1})/2$. At least we could numerically solve this equation and obtain a_1, b_1 . Similarly, we can get a_2, b_2 .

C Additional experiments

C.1 Training details

Forward filling irregularly sampled series. Each sample is comprised of the hourly values for a single patient's hospitalization. We identified 167,390 rows representing hourly values; after forward-filling and removing all entries which still contained at least one NA value, there were a total of 161,927 entries remaining, of which 80% is used as training data. The decision to forward fill was supported by clinical practices in which clinicians consider values meaningful for up to 24 hours from collection time. Furthermore, simple elimination of an NA containing row would result in the elimination nearly 2/3 of the available samples and would introduce significant bias.

The logistic regression model fitting is done by python function `LogisticRegression` in package `sklearn.linear_model`. A single patient's hospital stay can be divided into many smaller subsets, which reduces the prevalence of "sepsis-positive" windows. The training procedure is identical for each node; however, we detail the development of the Sepsis node below as this was the primary outcome of interest.

Forward feature selection. The forward feature selection is done by first fixing a small subset of features and then iteratively augmenting one feature to the subset until no performance gain can be achieved. The initial subset is determined jointly by random forest (python function `RandomForestClassifier`) feature importance and prior medical knowledge. Here, the performance (mainly TP rate, we also compare classification error and AUC) is evaluated on a testing dataset which is completely independent of the training dataset.

We should mention that this actually lead to significant performance improvement compared to both using all features and feature selection based on random forest feature importance. The feature importance ranking for node Sepsis is as follows:

```
ICULOS > Resp (min) > Temp (max) > Temp (mean) > MAP (min)
> HR (mean) > MAP (mean) > Resp (mean) > HR (max) > ... Shock
> O2Sat (min) > Inflammation > Renal Injury > ... > Cholestasis >
Oxygenation Dysfunction > Coagulopathy > Oxygen Carrying Dysfunction
> Diminished Cardiac Output > Electrolyte Imbalance > Hepatocellular
Injury
```

We can see this is very different from the features we select in the last two rows in Table 2. Our subset of features achieve better performance in terms of TP rate. During the forward selection process, the TP rate goes from around 0.6 up to final 0.768 whereas the TP rate for using all features

and subset selection based on random forest feature importance remain below 0.7. Our model achieve comparable performance (TP rate = 0.77 and AUC = 0.70) to sophisticated and commonly used prediction algorithm XGBoost (TP rate = 0.73 and AUC = 0.85).

Hyperparameter tuning. The hyperparameter is argument `max_iter`. We use this hyperparameter because the feature space is high-dimensional and early stop (instead of convergence) may lead to better generalization.

Imbalanced data. Among 5,222 patients, only 450 of them developed Sepsis during their ICU stay. To contend with this we use argument `class_weight='balanced'` to handle the issue of class imbalance.

Bootstrap confidence interval. We repeat the same procedure on a random sub-sample of the training data 1,000 times to create bootstrap samples of the logistic regression coefficients. Then we can construct level α confidence interval via $\alpha/2$ and $1 - \alpha/2$ quantiles of the bootstrap samples.

Table 4: Mean and standard deviation over bootstrap trials of the TP rate for each node in the graph.

	Sepsis	Renal Injury	Electrolyte Imbalance	Oxygen Carrying Dysfunction	Shock	Diminished Cardiac Output
Average TP rate	0.682436	0.730019	0.615018	0.695353	0.651345	0.59748
Standard deviation	0.035272	0.008189	0.058221	0.009539	0.012703	0.03640
	Coagulopathy	Cholestasis	Hepatocellular Injury	Oxygenation Dysfunction	Inflammation	
Average TP rate	0.638424	0.662546	0.622226	0.776112	0.712165	
Standard deviation	0.020609	0.011060	0.013895	0.009332	0.009308	

C.2 Additional results

We evaluated classification performance utilizing two separate CV metrics: TP rate (Figure 2) and classification error (Figure 7). Both approaches produce networks that demonstrate many conserved features, however, use of TP rate seems to place greater emphasis on clinically relevant relationships. For example the left graph in Figure 2 (i.e. maximizing TP rate with forward feature selection) shows greater involvement of the Renal node and slight differences in edge weights when compared to the left graph in Figure 7 (i.e. minimizing classification error). The same is also observed in the right graphs of Figure 2 and Figure 7 where forward feature selection is not used. For example maximizing TP rate seems to place more weight shock to cholestasis relationship which correlates with a well known clinical relationship. Ultimately maximizing TP during CV produces graphs that not only have a higher sensitivity for sepsis, but also seem to make more sense clinically.

To better elucidate the subtle relationships between nodes we also plot the non-thresholding version of Figures 2 and 7. In Figure 8 the effect of not performing feature selection becomes

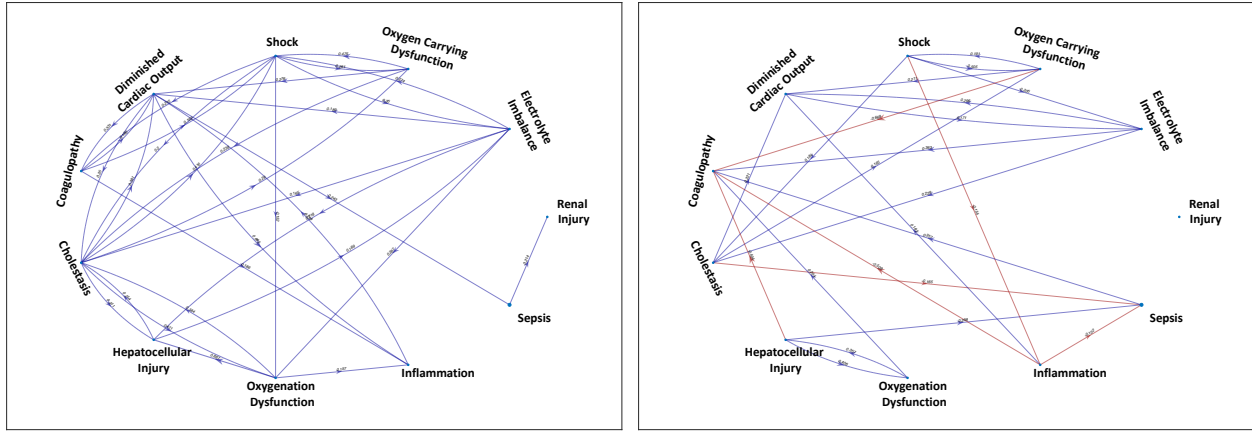


Figure 7: Bootstrap network topology with (left) and without (right) forward feature selection. We only keep (directed) edge with weight (logistic coefficient) whose absolute value is greater than 0.15. The blue (directed) edge indicates a positive effect whereas the red indicates a negative effect. The criterion for cross validation is true classification error (right).

evident as we can see numerous red edges indicating a inhibitory relationship between SAD nodes. From a physiologic perspective one would not normally expect a SAD to inhibit another SAD. While there could be unappreciated physiologic relationships or biases in the data that explain such an inhibitory relationship, these inhibitory relationships disappear (as seen in Figure 9) with feature selection suggesting that they are not meaningful and should be eliminated. The elimination of inhibitory relationships further highlights the importance of feature selection.

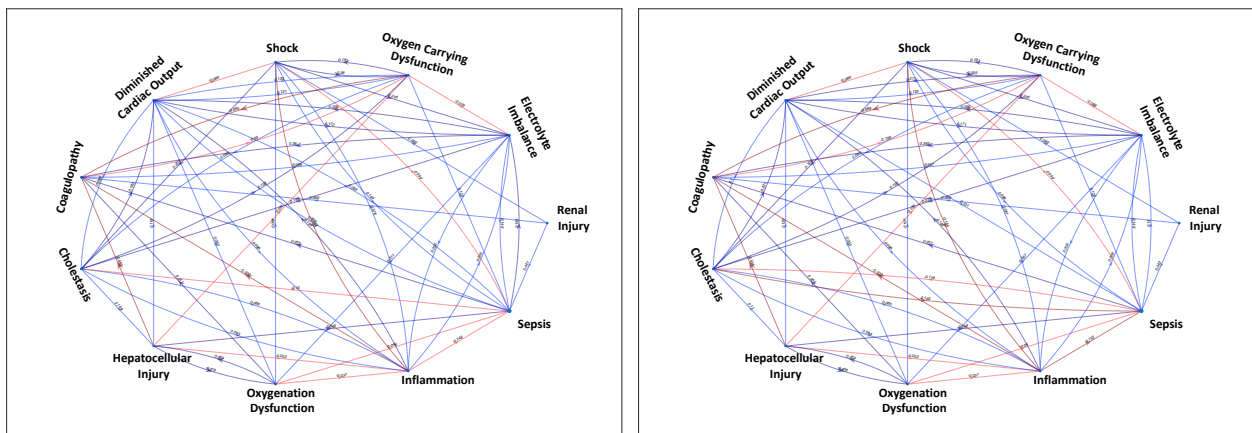


Figure 8: Bootstrap network topology WITHOUT feature selection. The blue (directed) edge indicates a positive effect whereas the red indicates a negative effect. The criterion for cross validation is true positive rate (left) and classification error (right).

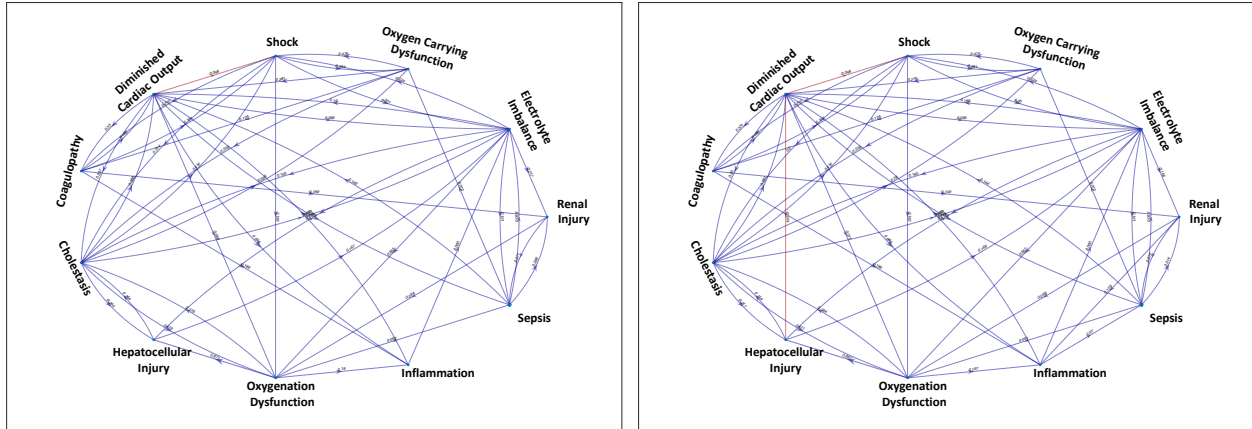


Figure 9: Bootstrap network topology WITH feature selection. The blue (directed) edge indicates a positive effect whereas the red indicates a negative effect. The criterion for cross validation is true positive rate (left) and classification error (right).

C.3 SVD clustering algorithm based on blockmodelling approach

Intuition. We first begin with intuition behind blockmodels; see Section 3 [Van Lierde et al., 2015] for a tutorial of clustering for directed graphs.

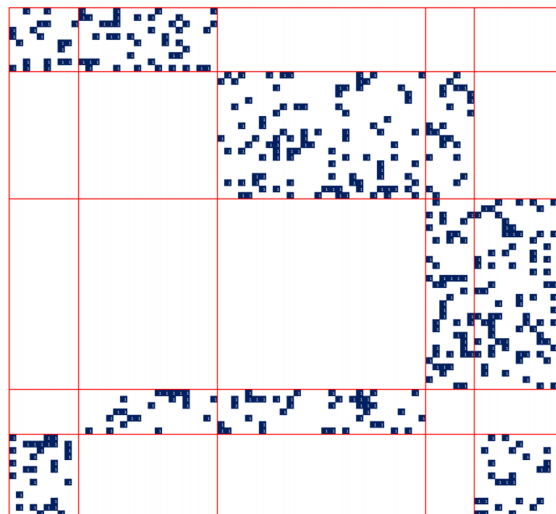


Figure 10: Illustration of Blockmodelling: Figure 1.4 [Van Lierde et al., 2015].

Intuitively, blockmodelling approaches are expected to detect block/cluster of nodes which are equivalent in terms of connections to other blocks/clusters. As illustrated in Figure 10 above, it can detect dense blocks in a sparse graph.

Spectral algorithm. Sussman et al. [2012] proposed a spectral algorithm to detect stochastic

blockmodels; this algorithm is based on singular value decomposition (SVD) of the adjacency matrix. See Algorithm 3 below.

Algorithm 3 Spectral Blockmodelling [Sussman et al., 2012].

Input: Adjacency matrix of undirected graph $W \in \{0, 1\}^{n \times n}$; hyperparameters d (number of blocks) and K (top K eigenvectors are kept after the SVD).

Step 1: SVD of adjacency matrix of undirected graph $W = U\Sigma V^T$, where Σ has decreasing main diagonal.

Step 2: Let \tilde{U}, \tilde{V} be the first d columns of U, V and let $\tilde{\Sigma}$ contain the first d columns and the first d rows of Σ .

Step 3: Define $\tilde{Z} = [\tilde{U}\tilde{\Sigma}^{1/2} | \tilde{V}\tilde{\Sigma}^{1/2}]$ by concatenation.

Step 4: Cluster the rows of \tilde{Z} using k-means algorithm with Euclidean distance.

Output: Estimation of block membership.
